Version of Record at: https://doi.org/10.1111/gbi.12551

Received: 4 November 2022 | Revised: 30 January 2023 | Accepted: 12 February 2023

DOI: 10.1111/gbi.12551

gebiology WILEY

ORIGINAL ARTICLE

The role of iron in the formation of Ediacaran 'death masks'

Brandt M. Gibson[1] | James D. Schiffbauer[2,3] | Adam F. Wallace[4] | Simon A. F. Darroch[1]

[1]Department of Earth & Environmental Sciences, Vanderbilt University, Nashville, Tennessee, USA

[2]Department of Geological Sciences, University of Missouri, Columbia, Missouri, USA

[3]X-ray Microanalysis Core Facility, University of Missouri, Columbia, Missouri, USA

[4]Department of Geological Sciences, University of Delaware, Newark, Delaware, USA

Correspondence
Brandt M. Gibson, Department of Earth & Environmental Sciences, Vanderbilt University, PMB 351805, 2301 Vanderbilt Place, Nashville, TN 37235-1805, USA.
Email: brandt.m.gibson@vanderbilt.edu

Funding information
Alexander von Humboldt-Stiftung; Geological Society of America, Grant/Award Number: GSRG-11444-16; National Science Foundation, Grant/Award Number: 1652351 and 1636643; Sigma Xi, Grant/Award Number: GIAR-G2017100194597859; Society for Sedimentary Geology; SEPM

Abstract

The Ediacara biota are an enigmatic group of Neoproterozoic soft-bodied fossils that mark the first major radiation of complex eukaryotic and macroscopic life. These fossils are thought to have been preserved via pyritic "death masks" mediated by seafloor microbial mats, though little about the chemical constraints of this preservational pathway is known, in particular surrounding the role of bioavailable iron in death mask formation and preservational fidelity. In this study, we perform decay experiments on both diploblastic and triploblastic animals under a range of simulated sedimentary iron concentrations, in order to characterize the role of iron in the preservation of Ediacaran organisms. After 28 days of decay, we demonstrate the first convincing "death masks" produced under experimental laboratory conditions composed of iron sulfide and probable oxide veneers. Moreover, our results demonstrate that the abundance of iron in experiments is not the sole control on death mask formation, but also tissue histology and the availability of nucleation sites. This illustrates that Ediacaran preservation via microbial death masks need not be a "perfect storm" of paleoenvironmental porewater and sediment chemistry, but instead can occur under a range of conditions.

KEYWORDS
organics, preservation, pyrite, sulfide, taphonomy

1 | INTRODUCTION

The Ediacara biota is an enigmatic group of soft-bodied fossils known from latest Neoproterozoic (~571–539 Ma) sediments worldwide. Despite recent advances in determining where several Ediacaran groups fit on the eukaryotic tree of life (Bobrovskiy et al., 2019; Dunn et al., 2017, 2021; Gold et al., 2015; Hoekzema et al., 2017; Schiffbauer et al., 2020), the majority possess uncertain relationships to extant metazoan groups, and thus their role in the Neoproterozoic rise of animals is still poorly understood (Darroch et al., 2018; Xiao & Laflamme, 2009). Understanding their phylogenetic relationships (if any) to extant animal groups are thus key to understanding both the early evolution of Metazoa and the origins of the modern marine biosphere (Darroch et al., 2018). One aspect that has continued to complicate our understanding of these fossils, however, is their unique mode of preservation.

Ediacaran soft tissues are preserved via several different taphonomic pathways, including—but not limited to—three-dimensional casts and molds in siliciclastic sediments (Callow & Brasier, 2009; Gehling, 1999; Narbonne, 2005) and as two-dimensional compressions (Anderson et al., 2011; Cai et al., 2010; Zhu et al., 2008). While compression-type preservation is well-known from numerous deposits throughout the Phanerozoic (Muscente et al., 2017), the once-dominant three-dimensional moldic mode of preservation,

prevalent in many Ediacaran localities, is largely absent outside of the Ediacaran Period (Gehling, 1999; Hagadorn & Bottjer, 1997; although see MacGabhann et al., 2019; Tarhan et al., 2016). This has led many authors to suggest that the cast and mold Ediacaran taphonomic pathway is controlled, at least to some degree, by common aspects of the Neoproterozoic paleoenvironments that change dramatically or disappear after the Cambrian boundary; for example, the composition of seawater (Tarhan et al., 2016) or the near-ubiquitous presence of seafloor microbial mats (Laflamme et al., 2011; Noffke, 2010; Noffke et al., 2002; Seilacher, 1999; Seilacher & Pflüger, 1994). Despite ~70 years of work, there remains uncertainty surrounding the pathway of Ediacaran fossil preservation; multiple models have been proposed, though their broader applicability and the ubiquity of each can be questioned based on differences between fossil deposits. Nonetheless, although recent models involving early silica cementation (Slagter et al., 2021; Tarhan et al., 2016) and sediment rheology (Bobrovskiy et al., 2019) have gained momentum, the leading hypothesis for over the past two decades remains the microbial "death mask" model (Droser et al., 2006; Gehling, 1999; Gehling et al., 2005; Liu et al., 2019).

The death mask model posits that soft-bodied Ediacaran organisms living in association with the microbial seafloor substrate were frequently buried by sediment during obrution events, such as during storm-influenced deposition. After burial, microbial mats recolonized the overlying sediment–water interface, preventing (or greatly limiting) the re-diffusion of oxygenated water downward into pore spaces surrounding the buried carcass. The onset of decay subsequently creates or amplifies anoxic conditions, which in turn reduces the rate of decay (Gehling, 1999; Gehling et al., 2005). Contemporaneously, sulfate-reducing bacteria (SRB) reduce seawater sulfate (SO_4^{2-}) to bisulfide (HS^-), which then reacts with pore water iron or reactive iron mineral phases (Canfield et al., 1992), followed by pyrite (FeS_2) (Berner, 1984; Raiswell et al., 1993). Lastly, carcass tissues and organics within surrounding sediments act as nucleation sites for pyrite formation, which molds the external surfaces of the organisms.

This model has received a wealth of both field and experimental support. For example, in South Australia, iron oxides and oxyhydroxides between bedding planes and fossil material have been interpreted as indicators of weathered pyrite (Gehling, 1999; Liu et al., 2019; although also see Tarhan et al., 2018 who interpret these as the result of late stage diagenesis); in Newfoundland, pyrite and iron oxides have been found inside clay layers surrounding fossils (Laflamme et al., 2011; Liu, 2016); and in the White Sea area of Russia, pyritized microbial filaments have been reported from the surfaces of Ediacaran fossils (Steiner & Reitner, 2001). Rudimentary death masks have also been experimentally produced in the laboratory. Darroch et al. (2012) decayed ecdysozoan larvae on freshwater microbial mats under simulated Ediacaran-style burial conditions, demonstrating the precipitation of sedimentary iron sulfides around decaying carcasses. Newman et al. (2019) performed an experimental decay study on scallop muscles, demonstrating the precipitation of iron-bearing phases within tissues resembling greigite and hematite. Lastly, in Ediacaran-style experimental decay of sea anemones and mollusks, Gibson et al. (2018) were able to demonstrate the precipitation of iron sulfide minerals in association with decaying organisms, but only after the addition of supplemental sedimentary iron. Under such conditions, they noted a morphological change from framboidal to blocky pyrite with increasing availability of sedimentary iron, leading them to question if iron may have been a key and limiting ingredient in death mask preservation. This hypothesis was further expanded, albeit hypothetically, by Schiffbauer et al. (2020) when discussing soft-tissue pyritization capturing an interpreted gut tract of an exceptionally preserved cloudinomorph fossil. While previous studies have assessed the influence of iron saturation levels on pyrite crystal forms (e.g., Murowchick & Barnes, 1987), few studies have done so at low temperature under taphonomic conditions. Gibson et al. (2018) suggested that the relatively fine crystal sizes of framboidal or indistinct globular pyrite may be optimal for preserving fine anatomical detail (and thus responsible for high-fidelity preservation of soft-bodied Ediacaran fossils), while the growth of blocky pyrite could overprint or obscure finer-scale features, and result in poorly preserved fossils with little recognizable anatomy. This transition from indistinct-to-framboidal habit to ordered cubic habit may be explained by an initial system of supersaturation—or at least large departure from equilibrium—to a system closer to equilibrium.

The combination of field and experimental evidence provides strong support for microbial death masks in many instances of Ediacaran fossil preservation, and hints at some control over preservation fidelity exerted by initial sedimentary/porewater iron concentrations. Here, we address the following specific questions as related to pyrite formation within the death mask model: (1) Is the initial availability of iron a limiting factor in the formation of superficial iron sulfide fossil coatings, akin to the death mask preservation model? (2) How does the initial iron abundance affect the length and fidelity of the death mask taphonomic window? and, (3) to what extent does the initial iron abundance affect the morphology of iron sulfides forming around carcasses? Addressing these questions will not only allow for a greater understanding of the formation of death masks and the extent to which they faithfully replicate the architecture of Ediacaran organisms, but will also test for the presence of facies- and paleoenvironment-based biases in Ediacaran fossil preservation that may be influencing our view of benthic ecosystems and eukaryotic evolution in the latest Precambrian.

We conducted a series of decay experiments on soft-bodied sea anemones and sea slugs in which we varied the initial abundance of sedimentary iron by total weight. As described below, we used fine-grained, zero valent iron powder, which does not directly replicate the presumed Ediacaran sedimentary environment but instead provides biologically available iron to jumpstart pyritization without the need for iron liberation via other microbial or chemical processes. We describe the degree of iron sulfide development on tissues and surrounding sediment and examine the relationship between initial iron abundance and the extent

of death mask formation using rates and patterns of organismal decay. Lastly, we discuss how these results fit into the larger context of Ediacaran death mask taphonomy.

2 | METHODS

As model organisms, we decayed actinian cnidarians (*Condylactis gigantea*, common name: the Caribbean Sea anemone) and shell-less gastropods (*Elysia crispata*, common name: the lettuce sea slug). We chose these organisms because of their similarities to previously studied Ediacaran decay analogues (Gibson et al., 2018; McMahon et al., 2017), and to incorporate both diploblastic and triploblastic organisms. Decay specimens were purchased from online retailers (Saltwaterfish.com; KPAquatics.com) and were typically ~1–6 cm in length. Following the protocols outlined in Gibson et al. (2018), all organisms were euthanized using magnesium chloride hexahydrate ($MgCl_2$*$6H_2O$) and then rinsed in Instant Ocean Artificial Seawater (specific gravity = 1.02; composition in Table S1). Replicates were decayed individually in separate 300 mL rectangular plastic decay vessels with lids. Microbial mats and sediment were collected on the western, sound side of Dauphin Island, AL, from an estuarine tidal flat with abundant mats comprised of cyanobacteria and sulfate-reducing bacteria (based on a typical purple to green-color vertical gradient; Vasconcelos et al., 2006). Medium to fine-grained (Figure S1) subangular quartz sand was also collected from approximately the same location. The quartzose composition of these sand grains was determined via visual assessment using microscopy. However, the abundance or composition of minor or accessory minerals was not determined. Prior to usage, it was dry sieved through a 1 mm mesh to remove larger organics (e.g., terrestrial plant material) that may have been present. Fine-grained zero valent iron (ZVI) powder (Sigma Aldrich 12310) was then hand-mixed via vigorous shaking with the sieved sand to specified iron percent weights (iron: sediment) representing a range by order and half-order increments from iron-poor (0.05%) to iron-rich (5.0%)—this provides an approximate match for Fe concentrations in natural systems, where 1–5 weight–percent iron can be found in siliclastic shales and organic-rich environments (Raiswell et al., 2018), although higher than those typically reported in sandstones. A thin layer of iron-mixed sediment was then placed in the bottom of each vessel. Microbial mat was placed on top of the iron-mixed sand, and decay replicates were then placed (Figure 1) on top of the mat. We then placed two layers of plastic film along the edges of the vessel to allow for easy separation later. By limiting the plastic film to the edges, free exchanges of decay fluids and anions/cations between the mat and overlying sediment were permitted. Additional sediment of the same iron content was then placed overtop the mat and decay specimens, and the entire vessel was inundated with Instant Ocean Artificial Seawater to the top of the vessel. Lastly, the vessels were sealed with lids, taking care to add additional seawater to remove any trapped air. Vessels were then placed in a Heracell VIOS i160 incubator to ensure consistent temperature, atmospheric composition, and humidity.

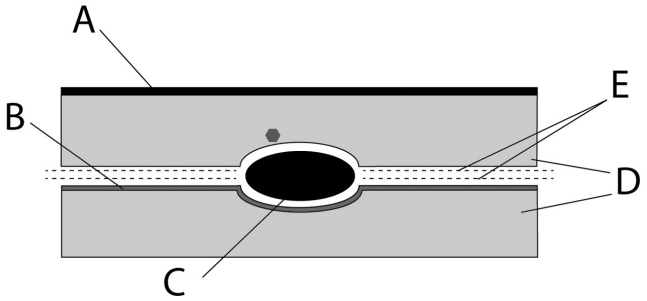

FIGURE 1 Illustrating experimental setup. (A) Lid cover sealing experiments and preventing gas with the broader environment within the incubator. (B) Mixed-species, sulfate reducing microbial mat. (C) Decay replicate. (D) Sand with supplemental iron. (E) Double layered plastic film with circle removed around organism. Gray hexahedron indicates locations of sediment retrieval per replicate.

Three replicates per iron percentage per species (n = 3) were removed from the incubator at timesteps of 7, 14, and 28 days (n = 18 per species per timestep; N = 108; Table S2). Vessels were immediately frozen to −81°C for storage until completion of the experiment to allow for analyzing specimens in a solid form (see methods of Darroch et al., 2012). After freezing, individual experiments were separated along the seam created by the two-layered plastic film. Remains were photographed, and broad anatomical characters scored for decay state following the decay stages outlined by Gibson et al. (2018). These characters include head and tentacle (i.e., anterior) tissues, outer dermis, inner musculature tissues, and the remaining internal "gut" or pharynx tissues (Gibson et al., 2018). Decay stages were established in quartile increments of recognizable tissue for the chosen anatomical characters that persisted (0%–25%, 25%–50%, 50%–75%, 75%–100% recognizable tissue loss). As shown in Figure 1, sediment samples were then collected from each experiment at the intersection of tissue and sediment. For a subset of experiments, we collected additional samples of the iron sulfide veneers that formed on the tissues, distinguishable by their metallic coloration. Sediment (and veneer) samples were affixed onto carbon disc adhesive-prepared aluminum stubs, with care taken to ensure nearly complete coverage of the carbon disc. No conductive sputter-coating was necessary because electron microscopy analyses were conducted in a variable pressure system at low vacuum, as further detailed below.

All geochemical analyses were conducted at the University of Missouri X-ray Microanalysis Core Facility (MizzoμX). Tissues and sediment were analyzed using scanning electron microscopy and energy-dispersive X-ray spectroscopy (SEM-EDS). These analyses were conducted using a Zeiss Sigma 500 variable-pressure SEM with dual, co-planar Bruker XFlash 6|30 silicon drift EDS detectors (30 mm^2 active window). All data were collected under identical operating conditions: low chamber vacuum (40 Pa) with a 99.999% N_2 atmosphere (allowing the samples to remain uncoated); 20 keV beam accelerating voltage; high current mode (40 nA probe current); and sample working distance of 8.5 mm.

Version of Record at: https://doi.org/10.1111/gbi.12551

Two different aperture settings were used: a 60 μm aperture was used during electron imaging, and a 120 μm aperture was used for X-ray spectroscopy to increase X-ray count rate. For imaging we used two detectors: a high definition five-segment backscattered electron detector (HDBSD; with all radial segments and the angular arm segment positively biased) for compositional imaging; and a cascade current detector (C2D; 30% bias applied) for topographic imaging (measuring the resulting current from an ionization cascade through the chamber gas). Images are a concurrent signal-mix from both detectors (75:25 [HDBSD:C2D]). Elemental mapping was conducted on each sample by using both co-planar EDS systems simultaneously to reduce shadow effects between affixed grains. Elemental mapping was conducted with a live time of 360 s, and at the described operating conditions yielded >250 kilocounts per second (kcps) combined between the two detectors. We collected area spectra and elemental maps for ~4.5 × 3.4 mm regions of interest (ROIs) on the prepared stubs. We specifically focused ROIs on dense sediment cover, which were typically located at the center of the stub unless it lacked adequate sediment coverage over the carbon tape. In such cases, the field of view was repositioned to the nearest area with dense sediment cover (aiming for ~80% coverage when possible). Full regional spectra were assessed from the elemental maps, and ZAF corrected and quantified using the Bruker ESPRIT 2 software package, with compositional results reported in normalized weight percentage. In all cases, a large proportion of the carbon signal resulted from the mounting adhesive. Co-occurrences of elements were visually assessed with maps compared side by side or using the enhanced mixing function in the Bruker ESPRIT software.

3 | RESULTS

We first describe the decay patterns for individual replicates over the duration of the experiment, organized by species and sediment iron abundance. We then describe the results of geochemical analyses, again split by species. Lastly, we document iron sulfide veneers that developed in some experiments.

3.1 | Sea anemone decay

Decay patterns and rates varied based on tissue type and were more rapid at higher initial iron availabilities. A comprehensive description of these patterns is presented in Text S1. Anterior (tentacles) and pharynx tissues decayed most rapidly, while muscle and dermal tissues typically persisted the longest. This pattern broadly follows those described by Gibson et al. (2018), whereby the thinnest tissues are the most labile and the thickest the most recalcitrant. Figure 2 illustrates decay patterns organized by iron abundance and shows the first and last occurrences of decay stages for broad-scale anatomical features. Due to the differential decay of replicates, later decay stages may first appear before the termination (and even onset) of earlier decay stages.

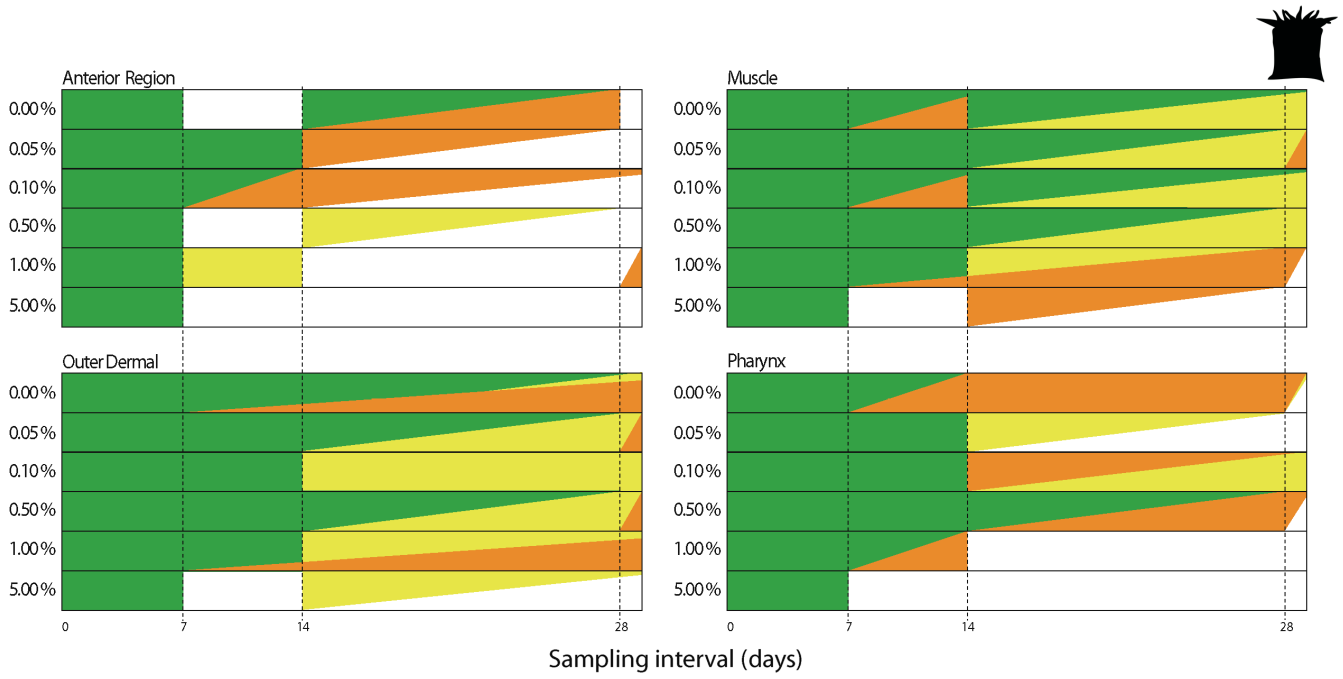

FIGURE 2 Pattern and temporal range of decay of diploblastic sea anemone (*Condylactis gigantea*) broken up by anatomical region ("characters") and scored using the decay stages outlined by Gibson et al. (2018); for each character, experiments using different starting abundances of Fe are stacked vertically. Colors indicate first and last occurrences of decay stages; green = 0%–25% loss of distinguishable tissue; yellow = 25%–50% loss of distinguishable tissue; orange = 50%–75% loss of distinguishable tissue; and white = 75%–100% loss of distinguishable tissue. Samples were collected on Days 7, 14, and 28.

Version of Record at: https://doi.org/10.1111/gbi.12551

3.2 | Sea slug decay

Similar to the sea anemones, the decay rates and patterns for sea slugs varied among iron percent weight groups. In contrast to the anemones, sea slug replicates for all iron percent weight groups saw whole features lost by the second time step (14 days). A comprehensive description of these patterns is also presented in Text S1. Similar to Figures 2 and 3 illustrates decay patterns in sea slugs organized by iron abundance and shows the first and last occurrences of decay stages for broad-scale anatomical features. As with the sea anemone decay, differential decay of sea slug replicates allowed for later decay stages to first appear before the termination (and even onset) of earlier decay stages.

3.3 | Geochemical characterization (sea anemones)

Normalized iron concentrations as observed by EDS show an increase, as expected, with increasing initial sedimentary iron (Figure S2). Figures S3–S5 show EDS spatial distribution data assessed from the sediment stubs. Sulfur was present in all replicates regardless of iron abundance or removal date. However, not all sediment samples exhibit spatial association between iron and sulfur; particularly, sediment samples from replicates removed early (e.g., 7 days) or those that had low concentrations of initial iron. With increasing initial iron abundance and longer decay intervals, the spatial co-occurrences of iron and sulfur also increased. More specifically, regions of spatial Fe–S overlap were consistently observed in association with organism-related carbon—typically the microbial mat or carcass tissue adhered to sediment grains—and was rarely found on sediment grains without the presence of carbon. Within Fe–S associations in the EDS maps, there are few mineral grains with recognizable framboid and/or blocky (e.g., cubic, octahedral, and pyritohedral) crystal habits (such as noted in Gibson et al., 2018). Most of the observed precipitates identified compositionally as iron sulfides lacked these commonly recognizable crystal forms, instead appearing as spherical to globular aggregates, or generally showing no distinctive external crystal shape, as observed in Figure 4. At lower initial iron abundances, Fe–S precipitates were smaller and generally more spherical in shape. Above 1.0% iron, precipitates became larger and transitioned in shape to more globular masses. While Fe–S spatial co-occurrences were more common later in the decay window, trends were also more ambiguous between iron abundance groups during this time. For all replicates below 0.1% at all sampling intervals, there was little spatial overlap between iron and sulfur in the EDS maps. While some co-occurrence is present at Day 7, most co-occurrences are first observed with Day 14, with the highest amount appearing on the samples removed on Day 28. Figure 4 shows mixed-signal overlays where Fe–S is present in direct association with organic C, most often forming along tabular microbial mat material.

3.4 | Geochemical characterization (sea slugs)

Similar to sea anemones, iron concentrations from elemental analyses increased with higher initial abundances of sedimentary iron

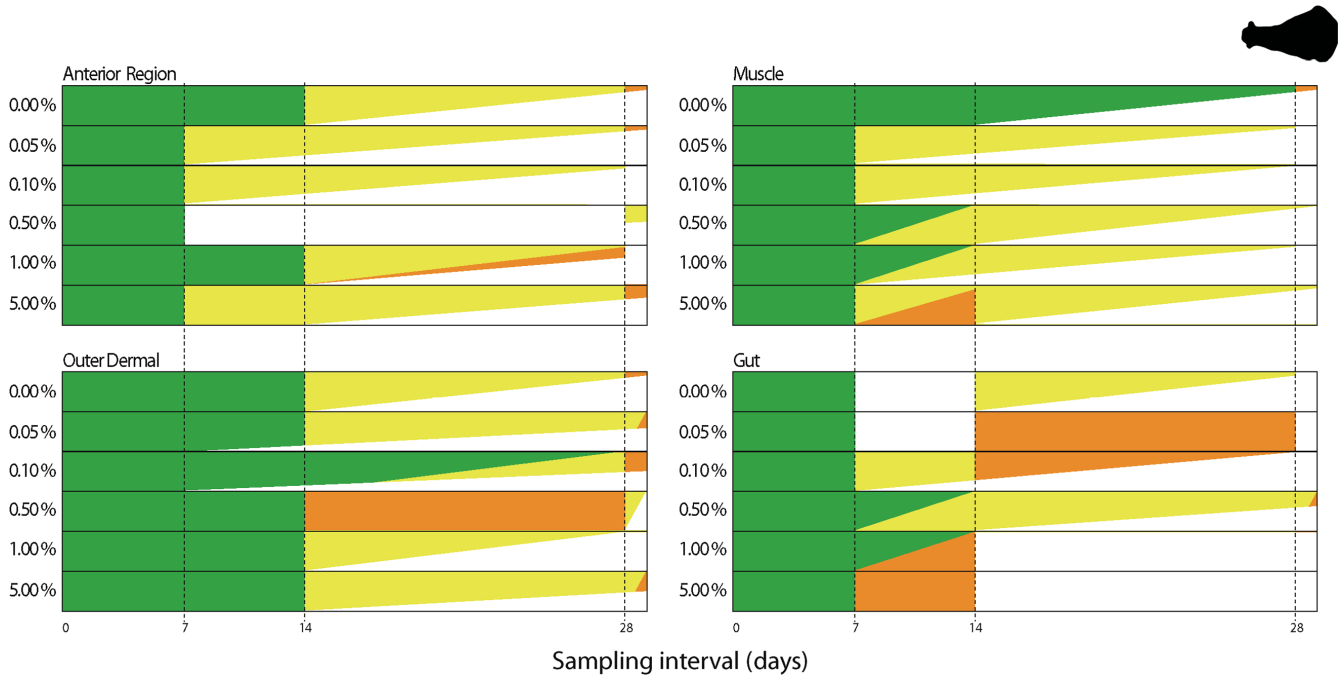

FIGURE 3 Pattern and temporal range of decay of triploblastic sea hare (*Elysia crispata*) broken up by anatomical region ("characters") and scored using the decay stages outlined by Gibson et al. (2018); for each character, experiments using different starting abundances of Fe are stacked vertically. Colors indicate first and last occurrences of decay stages; green = 0%–25% loss of distinguishable tissue; yellow = 25%–50% loss of distinguishable tissue; orange = 50%–75% loss of distinguishable tissue; and white = 75%–100% loss of distinguishable tissue. Samples were collected on Days 7, 14, and 28.

Version of Record at: https://doi.org/10.1111/gbi.12551

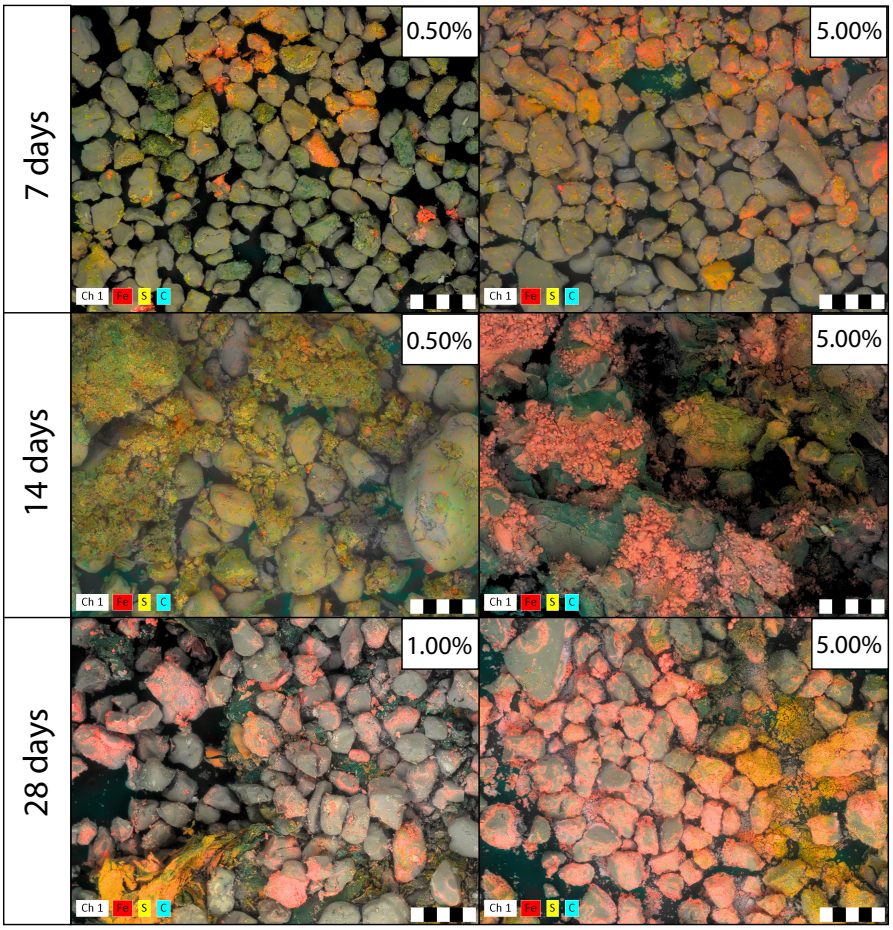

FIGURE 4 EDS maps of sediment surrounding decayed *Condylactis gigantea*. Percentages refer to initial iron abundance in starting experiments. Scale bar 200 μm.

(Figure S6). Figures S7–S9 show EDS maps for sea slugs. Sulfur associated with organic material was also present throughout samples regardless of supplemental iron abundance or decay length. Spatial associations between Fe and S were also observed within EDS maps for the sediment samples removed from sea slug replicates. Similar to the sea anemones, Fe–S spatial overlap typically increased with increasing decay length and with increased initial iron percent weight. Fe–S masses lacked notable crystalline shape, with some smaller spherical forms and larger globular accumulations. Also parallel to the anemones, Fe–S co-occurrences were localized to organics, as observed in the Fe–S + carbon EDS maps (Figure 5). More specifically, Fe–S associations were found on microbial mat or organics that had adhered to sediment grains, and precipitates were rarely found on grains lacking carbon.

3.5 | Iron sulfide veneers

Several replicates developed visible, macroscopic Fe–S veneers molding the surface of the carcass tissues (Figure 6) or regions of microbial mat. These veneers formed almost exclusively along tissue and mat surfaces with some isolated clumps forming further out from the sediment–tissue interface and forming along the sediment–mat interface (Figure 6). Veneers did not form in all replicates (only $n = 6$), instead forming almost exclusively in replicates with 1.0%–5.0% supplemental iron that were allowed to decay for 28 days (the exception being a partial veneer covering a sea anemone in 5.0% iron removed on Day 14). As shown in Figure 6c, Fe–S coated the surface of the microbial mat with additional sulfur coating the Fe–S veneer. Viewing the veneers at macroscale, they did not exhibit the rusty colors observed in the Gibson et al. (2018) experiments; instead, our veneers were a mixture of golden to lustrous white–golden (e.g., almost silver) in color (Figure 6).

4 | DISCUSSION

Iron sulfide veneers were observed coating organic surfaces in sea anemone replicates with 1.0%–5.0% initial iron weight percent, specifically forming along the intersection of carcass tissue, microbial mats, and the overlying sediment (Figures 5 and 6). While previous decay studies have successfully developed Fe–S associations (Darroch et al., 2012; Newman et al., 2019) and precipitated pyrite in various forms (Brock et al., 2006; Gibson et al., 2018; Grimes et al., 2001), this represents the first study to experimentally replicate coherent iron sulfide veneers along sediment–carcass

interfaces—broadly mimicking that proposed in death mask preservation of Ediacaran fossils. Here, we discuss the formation of these veneers and other Fe–S associations as they relate to the three questions that we had posed in Section 1.

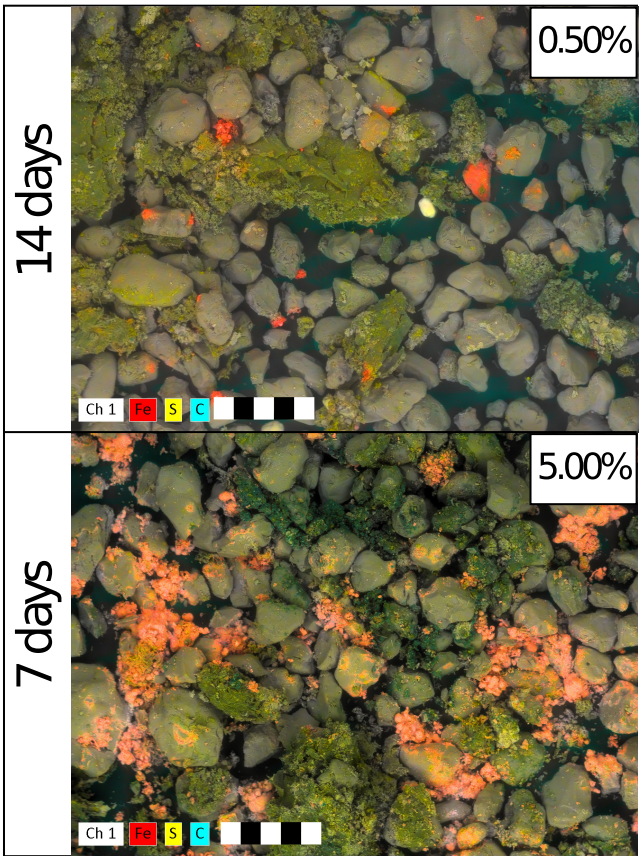

FIGURE 5 EDS maps of sediment surrounding decayed *Elysia crispata*. Percentages refer to initial iron abundance in starting experiments. Scale bar 200 μm.

4.1 | Question (1) Is the initial availability of iron a limiting factor in the formation of iron sulfide "death masks"?

The taphonomic experiments reported in Gibson et al. (2018) indicated that iron availability might exert a control on pyritic death mask preservation, but they were unable to test or quantify how much available iron was necessary for this taphonomic pathway. While minor and relatively rare Fe–S spatial associations were observed in our decay replicates with 0.05% iron-mixed sediment, Fe–S spatial associations were more consistently noticeable with starting iron percent weights ≥0.5%. Macroscopic iron sulfide veneers appear in experiments with initial iron percent weights ≥1.0%. Replicates from both test organisms demonstrate that increasing the initial available iron and length of time that the organisms are allowed to decay led to increased iron sulfide precipitation. Furthermore, our analyses and these data indicate that iron and sulfur also exhibit a strong spatial association with carbon (Figures S3–S5 and S7–S9), where Fe–S associations have formed almost exclusively on microbial mats or carcass tissues (Figures 4 and 5). Carcasses decayed in iron percent weights of <1.0% overwhelmingly formed iron sulfide precipitates associated with organic material, though Fe–S associations were not very extensive, and less spatial overlap was observed compared to replicates with higher initial iron abundances. Replicates decayed in sand with ≥1.0% supplemental iron developed Fe–S associations preferentially on organics but also developed growth along grains that appear to lack organics (compare panels in Figure 4). This is likely due to rapid exhaustion of the available organic nucleation sites (carcass tissue or microbial mat) while iron (from the supplemented powder) and sulfate levels are abundant in the porewater. Replicates decayed in sand with ≤0.1% supplemental iron did not develop consistently observable spatial overlap between iron and sulfur, indicating that there may be a lower limit on iron sulfide precipitation for sediments ≥0.5% iron, although this could be at least partly an artifact of the

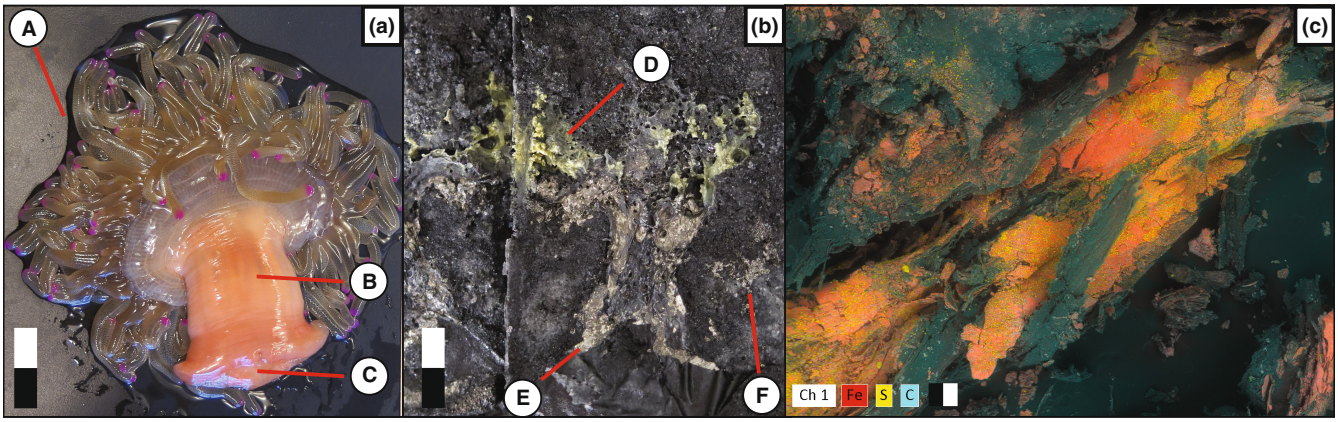

FIGURE 6 Images illustrating the decay of *Condylactis gigantea* tissue; (a) living sea anemone illustrating: (A) tentacles, (B) body column, and (C) foot. Scale bar 2 cm. (b) Pyritized tissue after 28 days in sediment with 1.0% Fe added, illustrating: (D) microbial biofilm coating tissues; (E) Fe–S veneer coating anemone foot tissue; (F) isolated Fe–S veneer developed on the sediment/mat surface. Scale bar 2 cm. (c) Energy dispersive spectroscopy map of an Fe–S veneer developed on a specimen of *C. gigantea* after 28 days decay in sediment with 5.0% Fe added. Scale bar 200 μm.

analytical protocol such that we are only observing limited sediments per replicate. Fe–S associations were almost exclusively found on organic surfaces (Figures 4 and 5; Figures S3–S5 and S7–S9) regardless of organism, suggesting that, while iron may be a limiting factor, the availability and suitability of organic surfaces to serve as nucleation sites for iron sulfides (Abraham, 1974; De Yoreo & Vekilov, 2003; Frankel & Bazylinski, 2003; Neilsen, 1967; Picard et al., 2018; Pósfai & Dunin-Borkowski, 2006; Wallace et al., 2009) is also a probable control for both death mask and pyritization preservation (Donald & Southam, 1999; Grimes et al., 2001; Rickard & Luther, 1997; Wilkins & Barnes, 1996). More generally, the occurrence of mineral nucleation and growth on a given substrate requires not only supersaturation in the immediate environment but also favorable interfacial energetics, which is to a large degree controlled by the nature of the substrate (Schiffbauer et al., 2014; Wallace et al., 2009). Lower interfacial energy favorable to substrate-mediated nucleation results where bonds between the mineral and the substrate are stronger than those between the mineral and the local solution phase (Abraham, 1974; Chernov, 1984; De Yoreo & Vekilov, 2003; Hamm et al., 2014; Mullin, 1992; Mutaftschiev, 1993; Neilsen, 1967) or where mineral deposition reduces the exposure of an energetically unfavorable substrate–solution interface (Giuffre et al., 2013). Even in the absence of significant bacterial sulfate reduction at the onset of burial, we speculate that iron begins to form associations with (what we assume to be) organic sulfhydryl groups associated with buried organisms, presenting a first layer of Fe–S before continued veneer growth fueled by rising HS^- from the decay activity of SRB. These results show agreement with the preservation of some organic tube-dwelling Ediacaran fossils (for example Schiffbauer et al., 2014, 2020).

We also note that zero valent iron powder (the Fe source used in these experiments) is not the form in which iron is typically stored in natural sediments. Thus, we cannot rule out that some of the sulfide generated during the decay period was produced by abiotic reduction of sulfate rather than by microbial activity. Therefore, the minimum Fe percent weights that were experimentally determined here may be different from real-world systems that would have iron sourced from reduction in natural oxidized archives or other reactive iron minerals, such as magnetite, hematite, siderite, and ankerite. Though the likely iron source(s) contributing to preservation in Ediacaran environments remain(s) unidentified, the degree of pyritization has been shown to be affected by elevated concentrations of iron minerals, such as iron oxyhydroxides, in sediments of modern marine environments (Canfield et al., 1992). In conjunction, our results lend further support to many previous studies that show optimality in the development of iron sulfides (see overview in Raiswell et al., 2018).

4.2 | Question (2) How does the initial iron abundance affect the length and fidelity of the death mask taphonomic window?

Absolute timescales for the development of iron sulfide aggregations will ultimately depend on the source of the iron (e.g., Fe-oxyhydroxides, hematite, magnetite, etc., as noted above), but our results using the sediments supplemented with zero valent iron powder show that percent weight does play an important role in the length and fidelity of the taphonomic window. The ZVI source used within these experiments likely expedites the early spatial associations between Fe–S, but more investigation comparing various natural sources of sedimentary iron is required to quantify these effects. An interesting observation was noted when tracking observable decay of replicates amongst differing initial iron percent weight groups. For both test organisms, the slowest loss of original biological characters to decay occurred in environments with intermediate iron percent weight groups (0.05%–0.5%). Replicates in the highest supplemental iron percent weight groups (1.0%–5.0%) yielded more observable decay starting with Day 14, as indicated here by large masses of spatially associated iron and sulfur on organic materials. The development of iron sulfide veneers superficially coating original tissues preferentially occurred in replicates with the highest iron percent weight groups (e.g., ≥1.0%). While the underlying cause is not entirely clear, environments with intermediate initial iron abundances appeared to be more conducive to slowing the processes of decay, while higher iron abundances with systems being further from equilibrium were more conducive to coating and masking the original carcass tissues with iron sulfides—both of which may be conducive to fossilization, though the latter provides a mechanism for initial mineral replacement or authigenic templating. We hypothesize that this process may have been similar to the structural biopolymer iron-adsorption model proposed by Petrovich (2001) in reference, instead, to the associations of fossil-related pyrite within both Burgess Shale-type compression fossils as well as pervasive, three-dimensional pyritization like that observed in the Frankfort Shale. Though there are notable differences in those depositional environments to those experimentally examined here, we hypothesize that this primary veneering could have been a result of early formation of iron–organosulfhydryl complexes upon burial, although we concede that this point requires further testing.

Our results also suggest there is an organismal disparity between the precipitation of iron sulfides and preservation potential. Replicates from both decay organisms developed iron sulfide precipitates, but greater qualitative preservation occurred in the sea anemone replicates, possibly due to larger tissue volumes or other histological controls. Sea anemone tentacles (anterior region) were, however, the most easily degradable and least likely to be preserved regardless of iron abundance. Replicates that did retain tentacles were typically found in experiments with lower iron abundances. This suggests that tentacle-type tissues/characters (or those that are highly labile soft tissues with a high surface area-to-volume ratio) are unlikely to be preserved regardless of the decay environment's ability to produce iron sulfides. This result supports suggestions made by Gibson et al. (2018) to the effect that the most labile tissues will rarely be preserved under death mask-type taphonomic scenarios (see also Hancy & Antcliffe, 2020). We also find that, by Day 28, tissue preservation in sea slugs was largely confined to the outer dermal tissue, regardless of iron abundance (also mimicking observations made by Gibson et al., 2018). This suggests that taphonomic mineralization of the outer tissue may act as a physical barrier to the preservation of

internal features (Gibson et al., 2018; Newman et al., 2019). In the context of our experiments, we suggest that adsorption of iron to exterior dermal tissues may have created nucleation sites for iron sulfides while also slowing decay by inhibiting enzymatic hydrolysis (Petrovich, 2001). This would in turn explain why internal features are often lost, while the external morphology of the organism is retained in the death mask preservational mode. In such cases where inner morphology is fossilized, the formation of iron sulfides must outpace the rate of decay of internal tissues, as recently discussed in Schiffbauer et al. (2020). There are plenty of other taphonomy-facilitating factors to consider as well that may contribute to the rate and pervasiveness of pyritization, such as limitation of disseminated organic matter in the sediment (e.g., Farrell et al., 2009) and diffusional controls on the availability of pore water iron (e.g., Hardisty et al., 2018; Raiswell et al., 1993; Schiffbauer et al., 2014), though these factors were not directly controlled-for in our experimental design. Nonetheless, it is at least possible that, if the experiment had progressed longer, the inner morphology may also have been preserved, but this is speculative and based on previous observations of temporally extended experiments (Gibson et al., 2018).

4.3 | Question (3) To what extent does the initial iron abundance affect the morphology of iron sulfides forming around carcasses?

Iron sulfide precipitates encasing soft tissues have been suggested to help preserve Ediacaran fossils in coarse-grained siliciclastic sediments. This model has been supported both by the presence of pyrite framboids directly on fossil surfaces, as well as associations between fossils and oxidative weathering products of iron sulfides (Gehling, 1999; Laflamme et al., 2011; Liu et al., 2019; Mapstone & McIlroy, 2006). Our Fe–S associations were consistently observed after 14 days of decay and become more apparent after 28 days of decay. While we did not observe the blocky pyrite noted in Gibson et al. (2018), we instead noted the presence of iron sulfides as both globules and smaller disseminated spherules likely informing system equilibrium/disequilibrium. However, death mask-type preservation is not dependent on the specific mineral morphologies of pyrite. Instead, a consistent superficial coating of iron sulfide phases on the outer surface of the decaying carcass—which we were able to produce in our laboratory setting—plausibly provides a higher potential for subsequent fossil preservation. While internal molds have been documented—particularly of holdfasts—(Bykova et al., 2017; Gehling et al., 2000; Tarhan et al., 2015)—these results also provide a feasible explanation for the preferential loss of internal anatomical structures in this taphonomic mode, where external molds of soft-bodied organisms are more favorably preserved (Gibson et al., 2018; Newman et al., 2019).

4.4 | Iron sulfide veneers

In addition to addressing our initial questions, the results of these experiments provide additional insights into putative death mask formation, specifically surrounding the nature of iron sulfide veneers on decaying organisms, the role of organic matter in providing nucleation sites for iron sulfide minerals, and the overall taphonomic pathway involved in death mask-type preservation. From our experiments, we observed the formation of Fe–S veneers on multiple experimental replicates, and over a range of iron percent weights, though only on anemone carcasses. These veneers superficially coat organic materials, usually of the organism's exterior dermis, thereby replicating its surface topography while thicker tissues such as muscles and the pharynx have been either flattened or been lost to decay. While macroscopically visible veneers did not form on sea slug carcasses, discrete Fe–S aggregates were present within the surrounding sand. The reasons underlying the disparity of veneer formation on sea anemones vs. sea hares remain unknown, though factors such as histology, lability of dermal tissues, and suitability for iron sulfide nucleation may play roles. Veneers that did form along the anemone carcass–sediment interfaces did not perfectly replicate their original tissue morphology, but instead often developed into textured surfaces that made the tissues appear deformed (Figure 6). Sea anemones decayed in sand in the highest iron percent weight groups developed macroscopically visible veneers by 28 days, broadly conforming to predictions from the original death mask hypothesis (Gehling, 1999). Our veneers and isolated Fe–S aggregates from the matrix sediments surrounding the carcasses of both sea anemone and sea slug replicates exhibit spherical and globular shapes instead of the anticipated framboidal or blocky (octahedron and cubic) morphologies observed by Gibson et al. (2018). This is because our Fe–S veneers were likely not coherent coatings of pyrite, and we instead suggest the veneers and other observed aggregates were likely amorphous or poorly crystalline iron sulfide precursors to pyrite or other undetermined iron sulfide mineral(s). Our results suggest that these precursors were likely playing the role of pyrite in the original death mask model, whereby they are coating and preserving external surfaces. Over geologic time these precursor phases would give way to more stable crystal forms but would still be important in facilitating early preservation. Importantly, their general presence appears more crucial for this taphonomic pathway than any specific thickness of their veneers. While these precursors were not determined to be pyrite, other iron sulfides (such as greigite—see e.g., Newman et al., 2019) have been suggested to also play a role in Ediacaran preservation.

4.5 | Role of organic nucleation sites

While pyrite and iron sulfide precursor formation can occur without a solid-phase substrate (e.g., Busigny et al., 2014), it has been suggested that the bulk of sedimentary iron sulfide mineral formation occurs as a result of microbially induced mineralization (e.g., Frankel & Bazylinski, 2003; Pósfai & Dunin-Borkowski, 2006). Explicitly, iron sulfide nucleation has been demonstrated to occur along organic surfaces, which provide sites for metal binding and mineral growth (Beveridge, 1989; Beveridge et al., 1983; Ferris et al., 1987; Fortin & Beveridge, 1997). More recently, the results

Version of Record at: https://doi.org/10.1111/gbi.12551

of experimentation conducted by Picard et al. (2018), for example, further demonstrate that both live and dead microbial cell surfaces as well as extracellular polymeric substances can serve as templates for the nucleation of iron sulfide minerals and favor their growth. In otherwise organic-limited sediments, these organotrophic microbes are likely to be utilizing the organics of the decaying organism as their primary electron donor, thus placing iron sulfide nucleation potential in direct proximity to the carcass tissues (as described by Raiswell et al., 1993).

Our results show a tendency for Fe–S associations to form along organic surfaces, with comparatively little Fe–S aggregation within the sediment. Spatial co-occurrences in our replicates were typically constrained to carcass surfaces rather than developing on microbial mat surfaces. Reconstructing the fossilization process for eldonids—enigmatic discoidal fossils characterized by a coiled sac—preserved in the Ordovician Tafilalt Lagerstätte of Morocco, MacGabhann et al. (2019) similarly noted that concentrations of iron along organic surfaces may inhibit decay by promoting authigenic mineralization. Under their model adsorption of Fe^{2+} would provide nucleation sites for the development of oxides (including iron oxides), which is in agreement with the results presented here. This also broadly agrees with results produced by Newman et al. (2019), whose experiments produced Fe–S enrichment within carcass tissues and found that microbial mats may not be required for three-dimensional death mask style preservation. There are, however, differences between Newman et al.'s results and ours. Principally, we show iron sulfides forming along the surface of tissues, instead of solely within tissues. We hypothesize that iron sulfides may concentrate in different locations based on tissue type, lability, and biochemistry, such as coating along smooth, non-porous tissues versus penetrating into more labile or porous tissues. It thus seems likely that nucleation rates strongly depend on the physiochemical properties of interfaces, where, for example, different underlying histologies or chemical terminations may promote nucleation and deposition (see also discussion of pyrite nucleation in Schiffbauer et al., 2014 and Raiswell et al., 1993).

4.6 | An expansion of the "death mask"-style taphonomic pathway

Our experiments provide insight into the types of mechanisms and timescales we might anticipate during death mask-type preservation. Our decay systems had an abundance of iron, organics, and sulfate, creating a scenario where Fe–S could form freely on organic surfaces. However, it is plausible that one or more of these conditions would have been limited in Ediacaran seafloor environments. If sulfate were limited (Brennan et al., 2004; Gill et al., 2007; Loyd et al., 2012), we might expect that Fe–S veneer formation would have been impeded, and tissues would have been lost entirely. Similarly, if porewater iron were scarce, we might anticipate that some preservation might occur, but this would be limited, and the majority of organic material would eventually decay entirely. Lastly, if organics were limited in an environment with abundant porewater iron and available sulfate, we might anticipate the carcass being entirely removed through

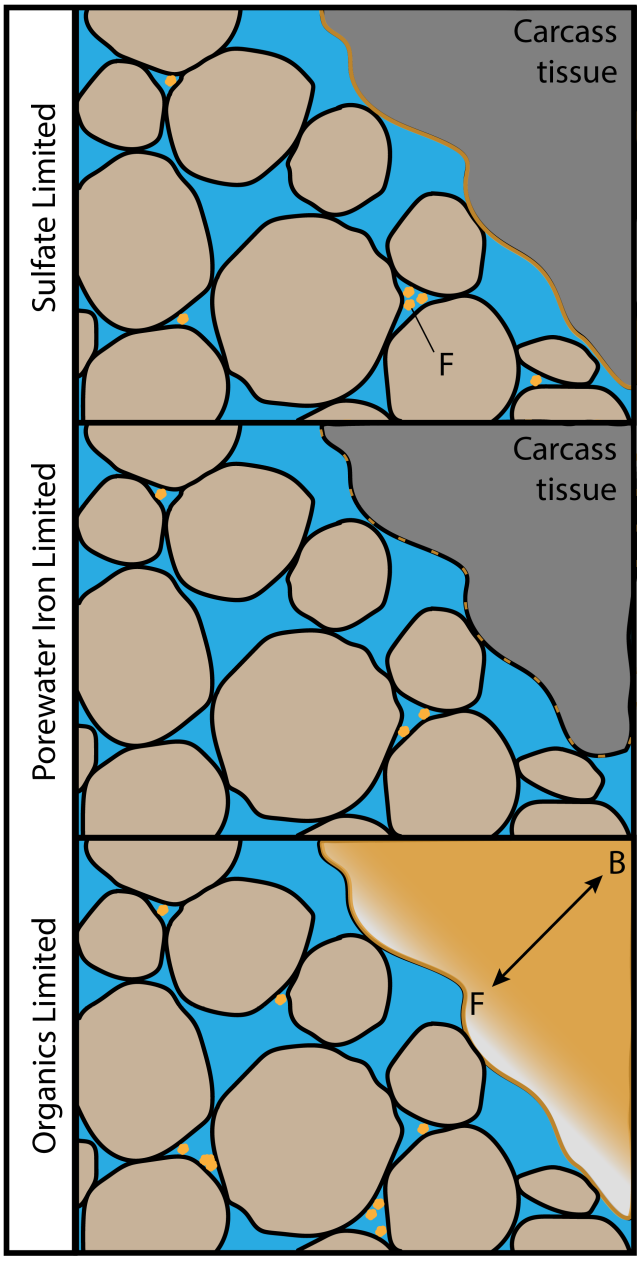

FIGURE 7 Alternative pathways for Ediacaran death mask preservation based on microenvironment conditions. Top: seawater sulfate limited in the presence of sufficient porewater iron and carcass organics yields Fe–S veneers along the carcass sediment surface and some inter-sediment grain pyrite framboids. Middle: limited porewater iron yields few sediment pyrite framboids (F) and causes limited veneer growth with the carcass ultimately completely decaying. Bottom: limited carcass organics in the presence of sufficient porewater iron and seawater sulfate yields the development of sediment pyrite framboids and significant replacement of carcass tissue with iron sulfides. A pyrite morphology gradient exists between the veneer/exterior (F: framboidal) and inner tissues (B: blocky).

decay, with Fe–S phases replacing the volume of decayed material (summarized in Figure 7).

Our results also demonstrate that the death mask model is not restricted to pyrite alone and could feasibly make use of other iron sulfide polymorphs that could mutually explain the presence of iron oxides and oxyhydroxides found in association with Ediacaran fossils (Liu, 2016; Liu et al., 2019). Previous work has suggested that microbial mats encourage (Slagter et al., 2022), but are not required for, Ediacaran preservation (Newman et al., 2019), demonstrating that this preservational pathway is pliable and thus able to occur under a larger variety of environmental conditions. Our results similarly suggest that this taphonomic pathway may not be as rigid as previously thought, ultimately not requiring a "perfect storm" of pore water microenvironmental and microbial substrate conditions, but instead possible under a wider variety of geochemical conditions and paleoenvironments.

4.7 | Ediacaran depositional environments and the death mask model

Pyrite formation after microbial sulfate reduction is mutually controlled by the availability of organic carbon, iron, and sulfur. Unoxidized Fe^{2+} has a lifespan of only minutes to hours in normal (standard temperatures, neutral pH, and moderate ionic strength; Millero et al., 1987) oxygenated waters, thus indicating that pyrite formation must occur in locally anoxic environments. If such environments are euxinic with high availability of sulfide, iron availability becomes the limiting factor for pyrite production (Berner, 1984; Raiswell et al., 2018; Raiswell & Berner, 1985). On the other hand, if the anoxic environment is also non-sulfidic, organic carbon becomes the limiting factor, serving as the primary electron donor for microbial sulfate reduction to convert sulfates to sulfides (Raiswell et al., 2018). Currently, there is no single agreed upon seawater chemistry model for the Ediacaran Ocean. For the global and deep ocean, several classic models suggest dominantly ferruginous waters (Canfield et al., 2008), euxinic waters (Shen et al., 2008; Wille et al., 2008), or combinations such as the "euxinic wedge" model where mid-depth water masses were variable products of oxic surface waters and ferruginous deep waters (Li et al., 2010). Recently, shallow waters of the Ediacaran have been reconstructed as mostly oxic with Ediacaran taxa inhibited by low-oxygen availability in underlying water masses (Tostevin et al., 2016). Under this model many Ediacaran organisms may have taken advantage of shallower oxygen refugia and as well as deeper and ephemerally oxic conditions that were typically more pervasively anoxic and euxinic water bodies. Support for this model has been interpreted from Fe speciation and trace fossil data of Namibia (Wood et al., 2015). More recently, geochemical data from several end Ediacaran basins support widespread euxinic conditions concentrated around productive continental margins with associated fossils suggesting that some sessile, soft-bodied Ediacara biota were capable of thriving in low-oxygen environments (Cherry et al., 2022). Under this euxinic model, greater oxygenation of the ocean to more modern levels may have occurred well into the Phanerozoic (Lu et al., 2018; Wallace et al., 2017).

Our results support the notion that iron played an important role in death mask-type preservation. For the systems that we created, veneers formed in treatment groups >1.0 weight percent iron. In natural systems, 1–5 weight-percent iron can be found in siliclastic shales and organic rich environments (Raiswell et al., 2018), but this is less common in modern sandstones and carbonates (Clarkson et al., 2014). Wollanke and Zimmerle (1990) suggest that montmorillonite-rich sediments or volcanic ash (basaltic Fe_2O_3 weights can get as high as 3.8%) might supply iron for Ediacaran preservation, such as has been suggested at Mistaken Point (Liu, 2016; Petrovich, 2001). In the Rawnsley Quartzite Ediacara Member, cemented and uncemented quartz grains are coated with iron (III) oxide or oxyhydroxide (Wade, 1968; although see Tarhan et al., 2016), which could suggest non-negligible amounts of porewater iron (Petrovich, 2001). Assuming local suboxic conditions during death mask-type preservation, the question regarding the source of iron remains unanswered. However, the inference that a threshold level of iron may be required for death mask formation raises the possibility of a facies bias in fossil preservation, with fossils of soft-bodied Ediacara biota preferentially forming in depositional systems characterized iron percentages above this threshold. This may help explain, for example, why Ediacara biota are relatively common in siliciclastic settings, but comparatively rare (although not totally absent) in carbonate settings where iron is less abundant (Chen et al., 2014).

Finally, although we argue that our study provides more evidence for a pyritic "death mask" model for Ediacaran preservation, building on both observational (Gehling, 1999; Laflamme et al., 2011; Liu et al., 2019) and experimental (Darroch et al., 2012; Gibson et al., 2018) data, we note that this taphonomic pathway was likely not operating to the exclusion of all others. Previous studies have noted that there is unlikely to be one single taphonomic pathway responsible for the preservation of soft-bodied Ediacara biota (MacGabhann, 2014; Narbonne, 2005), and the preservational disparity evident among many individual taxa supports this (e.g., MacGabhann et al., 2019). In particular, Tarhan et al. (2016, 2018, 2019) have documented a paucity of pyrite and oxide grain coatings across Rawnsley Quartzite Ediacara Member sediments at Nilpena—one of the richest Ediacaran fossil sites known—and instead propose a taphonomic model centered around early silicification (with experimental support given by Slagter et al., 2021). On the basis of similar observations—in addition to a lack of silicic cement surrounding fossils—Bobrovskiy et al. (2019) proposed a model based around sediment rheology. Our results thus demonstrate that pyritic death masks represent a plausible taphonomic pathway for soft-bodied Ediacaran fossils (and explain many of the morphological and geochemical characteristics of fossils) but do not preclude a variety of pathways from operating in different localities and settings.

5 | CONCLUSIONS

The results of these experiments demonstrate that, while a source of iron is required for death mask-style preservation, its presence alone is not sufficient to guarantee death mask formation. Instead,

death mask-type preservation may result from a combination of available iron, seawater sulfate and sulfate-reducing microbes, and the presence of nucleation sites for building iron sulfide minerals. These results represent the first truly Ediacaran-looking Fe–S veneers precipitated under laboratory conditions, and suggest this process begins within the first few weeks of decay. While these veneers are more likely amorphous or poorly crystalline precursors to pyrite, the development and ability of these phases to superficially coat tissue morphology demonstrates the merits and feasibility of Gehling's (1999) death mask model. Thus, while death masks may not be the sole mechanism of soft-tissue preservation in the latest Neoproterozoic (see e.g., Bobrovskiy et al., 2019; Tarhan et al., 2016), we demonstrate that death mask formation can be replicated in the laboratory under a range of conditions and explains the character of many fossils in Ediacaran-aged deposits worldwide.

ACKNOWLEDGMENTS

The authors would like to thank Elli Ronay, Eva Biedron, Lydia Harmon, and Matthew Dietrich for assistance in the lab. BMG was supported by the Geological Society of America GSRG-11444-16, SEPM (Graduate Student Research Grant), and Sigma Xi GIAR-G2017100194597859. JDS is supported by NSF EAR CAREER-1652351 and acknowledges support of the X-ray Microanalysis Core Facility by NSF EAR I&F-1636643. S.A.F.D. acknowledges a travel grant from the Southeastern Conference as well as generous support from the Alexander von Humboldt Foundation, which is sponsored by the Federal Ministry for Education and Research in Germany. We would like to thank three anonymous reviewers and Subject Editor Lidya Tarhan for comments and additions to the manuscript.

DATA AVAILABILITY STATEMENT

The data that supports the findings of this study are available in the supplementary material of this article.

ORCID

Brandt M. Gibson https://orcid.org/0000-0001-9620-0063
James D. Schiffbauer https://orcid.org/0000-0003-4726-0355

REFERENCES

Abraham, F. F. (1974). *Homogeneous nucleation theory*. Academic Press.

Anderson, E. P., Schiffbauer, J. D., & Xiao, S. (2011). Taphonomic study of Ediacaran organic-walled fossils confirms the importance of clay minerals and pyrite in Burgess Shale-type preservation. *Geology*, *39*, 643–646. https://doi.org/10.1130/G31969.1

Berner, R. A. (1984). Sedimentary pyrite formation: An update. *Geochimica et Cosmochimica Acta*, *48*, 605–615.

Beveridge, T. J. (1989). Role of cellular design in bacterial metal accumulation and mineralization. *Annual Review of Microbiology*, *43*, 147–171.

Beveridge, T. J., Meloche, J. D., Fyfe, W. S., & Murray, R. G. E. (1983). Diagenesis of metals chemically complexed to bacteria: Laboratory formation of metal phosphates, sulfides, and organic condensates in artificial seawater. *Applied and Environmental Microbiology*, *45*, 1094–1108.

Bobrovskiy, I., Krasnova, A., Ivantsov, A., Luzhnaya (Serezhnikova), E., & Brocks, J. J. (2019). Simple sediment rheology explains the Ediacara biota preservation. *Nature Ecology & Evolution*, *3*, 582–589. https://doi.org/10.1038/s41559-019-0820-7

Brennan, S. T., Lowenstein, T. K., & Horita, J. (2004). Seawater chemistry and the advent of biocalcification. *Geology*, *32*, 473–476.

Brock, F., Parkes, R. J., & Briggs, D. E. G. (2006). Experimental pyrite formation associated with decay of plant material. *PALAIOS*, *21*, 499–506.

Busigny, V., Planavsky, N. J., Jézéquel, D., Crowe, S., Louvat, P., Moureau, J., Viollier, E., & Lyons, T. W. (2014). Iron isotopes is an Archean Ocean analogue. *Geochimica et Cosmochimica Acta*, *133*, 443–463. https://doi.org/10.1016/j.gca.2014.03.004

Bykova, N., Gill, B. C., Grazhdankin, D., Rogov, V., & Xiao, S. (2017). A geochemical study of the Ediacaran discoidal fossil Aspidella preserved in limestones: Implications for its taphonomy and paleoecology. *Geobiology*, *15*(4), 572–587. Portico. https://doi.org/10.1111/gbi.12240

Cai, Y., Hua, H., Xiao, S., Schiffbauer, J. D., & Li, P. (2010). Biostratinomy of the late Ediacaran pyritized Gaojiashan Lagerstätte from southern Shaanxi, South China: Importance of event deposits. *PALAIOS*, *25*, 487–506. https://doi.org/10.2110/palo.2009.p09-133r

Callow, R. H. T., & Brasier, M. D. (2009). Remarkable preservation of microbial mats in Neoproterozoic siliciclastic settings: Implications for Ediacaran taphonomic models. *Earth Science Reviews*, *96*, 207–219. https://doi.org/10.1016/j.earscirev.2009.07.002

Canfield, D. E., Poulton, S. W., Knoll, A. H., Narbonne, G. M., Ross, G., Goldberg, T., & Strauss, H. (2008). Ferruginous conditions dominated later neoproterozoic deep-water chemistry. *Science*, *321*(5891), 949–952. https://doi.org/10.1126/science.1154499

Canfield, D. E., Raiswell, R., & Bottrell, S. (1992). The reactivity of sedimentary iron minerals toward sulfide. *American Journal of Science*, *292*, 659–683.

Chen, Z., Zhou, C., Xiao, S., Wang, W., Guan, C., Hua, H., & Yuan, X. (2014). New Ediacara fossils preserved in marine limestone and their ecological implications. *Scientific Reports*, *4*, 4180.

Chernov, A. A. (1984). *Modern crystallography III: Crystal growth*. Springer.

Cherry, L. B., Geilleaudeau, G. J., Grazhdankin, D. M., Romaniello, S. J., Martin, A. J., & Kaufman, A. J. (2022). A diverse Ediacara assemblage survived under low-oxygen conditions. *Nature Communications*, *13*, 1–11. https://doi.org/10.1038/s41467-022-35012-y

Clarkson, M. O., Poulton, S. W., Guilbaud, R., & Wood, R. A. (2014). Assessing the utility of Fe/Al and Fe-speciation to record water column redox conditions in carbonate-rich sediments. *Chemical Geology*, *382*, 111–122. https://doi.org/10.1016/j.chemgeo.2014.05.031

Darroch, S. A. F., Laflamme, M., Schiffbauer, J. D., & Briggs, D. E. G. (2012). Experimental formation of a microbial death mask. *PALAIOS*, *27*, 293–303. https://doi.org/10.2110/palo.2011.p11-059r

Darroch, S. A. F., Smith, E. F., Laflamme, M., & Erwin, D. H. (2018). Ediacaran extinction and Cambrian explosion. *Trends in Ecology & Evolution*, *33*, 653–663.

De Yoreo, J. J., & Vekilov, P. G. (2003). Principles of crystal nucleation and growth. *Reviews in Mineralogy and Geochemistry*, *54*, 57–93. https://doi.org/10.2113/0540057

Donald, R., & Southam, G. (1999). Low temperature anaerobic bacterial diagenesis of ferrous monosulphide to pyrite. *Geochimica et Cosmochimica Acta*, *63*, 2019–2023.

Droser, M. L., Gehling, J. G., & Jensen, S. R. (2006). Assemblage palaeoecology of the Ediacara biota: The unabridged edition? *Palaeogeography, Palaeoclimatology, Palaeoecology*, *232*, 131–147. https://doi.org/10.1016/j.palaco.2005.12.015

Dunn, F. S., Liu, A. G., & Donoghue, P. C. J. (2017). Ediacaran developmental biology. *Biological Reviews*, *93*(2), 914–932. Portico. https://doi.org/10.1111/brv.12379

Dunn, F. S., Liu, A. G., Grazhdankin, D. V., Vixseboxse, P., Flannery-Sutherland, J., Green, E., Harris, S., Wilby, P. R., & Donoghue, P. C. J. (2021). The developmental biology of *Charnia* and the eumetazoan affinity of the Ediacaran rangeomorphs. *Science Advances*, *7*, 1–13. https://doi.org/10.1126/sciadv.abe0291

Farrell, Ú. C., Martin, M. J., Hagadorn, J. W., Whiteley, T., & Briggs, D. E. G. (2009). Beyond Beecher's trilobite bed; widespread pyritization of soft tissues in the Late Ordovician Taconic foreland basin. *Geology*, *37*, 907–910.

Ferris, F. G., Fyfe, W. S., & Beveridge, T. J. (1987). Bacteria as nucleation sites for authigenic mineral sin a metal-contaminated lake sediment. *Chemical Geology*, *63*, 225–232.

Fortin, D., & Beveridge, T. J. (1997). Microbial sulfate reduction within sulfidic mine tailings: Formation of diagenetic Fe sulfides. *Geomicrobiology Journal*, *14*, 1–21.

Frankel, R. B., & Bazylinski, D. A. (2003). Biologically induced mineralization by bacteria. *Reviews in Mineralogy and Geochemistry*, *54*, 95–114.

Gehling, J. G. (1999). Microbial mats in terminal Proterozoic siliciclastics: Ediacaran death masks. *PALAIOS*, *14*(1), 40–57.

Gehling, J. G., Droser, M. L., Jensen, S. R., & Runnegar, B. N. (2005). Ediacara organisms: Relating form to function. In D. E. G. Briggs (Ed.), *Evolving form and function: Fossils and development: Proceedings of a symposium honoring Adolf Seilacher for his contributions to paleontology, in Celebration of his 80th birthday* (288 pp). Yale University.

Gehling, J. G., Narbonne, G., & Anderson, M. (2000). The first named Ediacaran body fossil, *Aspidella terranovica*. *Palaeontology*, *43*, 427–456.

Gibson, B. M., Schiffbauer, J. D., & Darroch, S. A. F. (2018). Ediacaran-style decay experiments using mollusks and sea anemones. *PALAIOS*, *33*, 185–203. https://doi.org/10.2110/palo.2017.091

Gill, B. C., Lyons, T. W., & Saltzman, M. R. (2007). Parallel, high-resolution carbon and sulfur isotope records of the evolving Paleozoic marine sulfur reservoir. *Palaeogeography, Palaeoclimatology, Palaeoecology*, *256*, 156–173.

Giuffre, A. J., Hamm, L. M., Han, N., De Yoreo, J. J., & Dove, P. M. (2013). Polysaccharide chemistry regulates kinetics of calcite nucleation through competition of interfacial energies. *Proceedings National Academy of Sciences of the United States of America*, *110*, 9261–9266. https://doi.org/10.1073/pnas.1222162110

Gold, D. A., Runnegar, B., Gehling, J. G., & Jacobs, D. K. (2015). Ancestral state reconstruction of ontogeny supports a bilaterian affinity for *Dickinsonia*. *Evolution & Development*, *17*, 315–324. https://doi.org/10.1111/ede.12168

Grimes, S. T., Brock, F., Rickard, D., Davies, K. L., Edwards, D., & Briggs, D. E. G. (2001). Understanding fossilization: Experimental pyritization of plants. *Geology*, *29*, 123–126. https://doi.org/10.1130/0091-7613(2001)029<0123:UFEPOP>2.0.CO;2

Hagadorn, J. W., & Bottjer, D. J. (1997). Wrinkle structures: Microbially mediated sedimentary structures common in subtidal siliciclastic settings at the Proterozoic-phanerozoic transition. *Geology*, *25*, 1047–1050.

Hamm, L. M., Giuffre, A. J., Han, N., Tao, J., Wang, D., De Yoreo, J. J., & Dove, P. M. (2014). Reconciling disparate views of template-directed nucleation through measurement of calcite nucleation kinetics and binding energies. *Proceedings National Academy of Sciences of the United States of America*, *111*, 1304–1309. https://doi.org/10.1073/pnas.1312369111

Hancy, A. D., & Antcliffe, J. B. (2020). Anoxia can increase the rate of decay for cnidarian tissue: Using *Actinia equina* to understand the early fossil record. *Geobiology*, *18*, 167–184. https://doi.org/10.1111/gbi.12370

Hardisty, D. S., Lyons, T. W., Riedinger, N., Isson, T. T., Owens, J. D., Aller, R. C., Rye, D. M., Planavsky, N. J., Reinhard, C. T., Gill, B. C., Masterson, A. L., Asael, D., & Johnston, D. T. (2018). An evaluation of sedimentary molybdenum and iron as proxies for pore fluid paleoredox conditions. *American Journal of Science*, *318*, 527–566. https://doi.org/10.2475/05.2018.04

Hoekzema, R. S., Brasier, M. D., Dunn, F. S., & Liu, A. G. (2017). Quantitative study of developmental biology confirms *Dickinsonia* as a metazoan. *Proceedings of the Royal Society B: Biological Sciences*, *284*, 20171348. https://doi.org/10.1098/rspb.2017.1348

Laflamme, M., Schiffbauer, J. D., Narbonne, G. M., & Briggs, D. E. G. (2011). Microbial biofilms and the preservation of the Ediacara biota. *Lethaia*, *44*, 203–213. https://doi.org/10.1111/j.1502-3931.2010.00235.x

Li, C., Love, G. D., Lyons, T. W., Fike, D. A., Sessions, A. L., & Chu, X. (2010). A stratified redox model for the Ediacaran Ocean. *Science*, *328*, 80–83.

Liu, A. G. (2016). Framboidal pyrite shroud confirms the 'death mask' model for moldic preservation of Ediacaran soft-bodied organisms. *PALAIOS*, *31*, 259–274. https://doi.org/10.2110/palo.2015.095

Liu, A. G., McMahon, S., Matthews, J. J., Still, J. W., & Brasier, A. T. (2019). Petrological evidence supports the death mask model for the preservation of Ediacaran soft-bodied organisms in South Australia. *Geology*, *47*, 215–218. https://doi.org/10.1130/G45918.1/4617348/g45918

Loyd, S. J., Marenco, P. J., Hagadorn, J. W., Lyons, T. W., Kaufman, A. J., Sour-Tovar, F., & Corsetti, F. A. (2012). Sustained low marine sulfate concentrations from the Neoproterozoic to the Cambrian: Insights from carbonates of northwestern Mexico and eastern California. *Earth and Planetary Science Letters*, *339*, 79–94.

Lu, W., Ridgwell, A., Thomas, E., Hardisty, D. S., Luo, G., Algeo, T. J., Saltzman, M. R., Gill, B. C., Shen, Y., Ling, H., Edwards, C. T., Whalen, M. T., Zhou, X., Gutchess, K. M., Jin, L., Rickaby, R. E. M., Jenkyns, H. C., Lyons, T. W., Lenton, T. M., … Lu, Z. (2018). Late inception of a resiliently oxygenated upper ocean. *Science*, *361*, 174–177. https://doi.org/10.1126/science.aar5372

MacGabhann, B. A. (2014). There's no such thing as the Ediacara biota. *Geoscience Frontiers*, *5*, 53–62. https://doi.org/10.1016/j.gsf2013.08.001

MacGabhann, B. A., Schiffbauer, J. D., Hagadorn, J. W., Roy, P. V., Lynch, E. P., Morrison, L., & Murray, J. (2019). Resolution of the earliest metazoan record: Differential taphonomy of Ediacaran and Paleozoic fossil molds and casts. *Palaeogeography, Palaeoclimatology, Palaeoecology*, *513*, 146–165. https://doi.org/10.1016/j.palaeo.2018.11.009

Mapstone, N. B., & McIlroy, D. (2006). Ediacaran fossil preservation: Taphonomy and diagenesis of a discoid biota from the Amadeus Basin, Central Australia. *Precambrian Research*, *149*, 126–148.

McMahon, S., Tarhan, L. G., & Briggs, D. E. G. (2017). Decay of the sea anemone *Metridium* (Actiniaria): Implications for the preservation of cnidarian polyps and other soft-bodied diploblast-grade animals. *PALAIOS*, *32*, 388–395. https://doi.org/10.2110/palo.2016.102

Millero, F. J., Sotolongo, S., & Izaguirre, M. (1987). The oxidation kinetics of Fe(II) in seawater. *Geochimica et Cosmochimica Acta*, *5*, 793–801.

Mullin, J. W. (1992). *Crystallization* (3rd ed.). Butterworths.

Murowchick, J. B., & Barnes, H. L. (1987). Effects of temperature and degree of supersaturation on pyrite morphology. *American Mineralogist*, *72*, 1241–1250.

Muscente, A. D., Schiffbauer, J. D., Broce, J., Laflamme, M., O'Donnell, K., Boag, T. H., Meyer, M., Hawkins, A. D., Huntley, J. W., McNamara, M., MacKenzie, L. A., Stanley, G. D., Jr., Hinman, N. W., Hofmann, M. H., & Xiao, S. (2017). Exceptionally preserved fossil assemblages through geologic time and space. *Gondwana Research*, *48*, 168–188.

Mutaftschiev, B. (1993). Nucleation. In D. T. J. Hurle (Ed.), *Handbook on crystal growth* (pp. 189–247). North-Holland.

Narbonne, G. M. (2005). The Ediacara biota: Neoproterozoic origin of animals and their ecosystems. *Annual Review of Earth and Planetary Sciences*, *33*, 421–422. https://doi.org/10.1146/annurev.earth.33.092203.122519

Neilsen, A. E. (1967). Nucleation in aqueous solutions. In S. Peiser (Ed.), *Crystal growth* (pp. 419–426). Pergamon.

Newman, S. A., Daye, M., Fakra, S. C., Marcus, M. A., Pajusalu, M., Pruss, S. B., Smith, E. F., & Bosak, T. (2019). Experimental formation of muscle tissue in quartz sand and kaolinite. *PALAIOS*, *34*, 437–451. https://doi.org/10.2110/palo.2019.030

Noffke, N. (2010). *Geobiology: Microbial mats in sandy deposits from the Archean era to today* (194 pp). Springer-Verlag.

Noffke, N., Knoll, A. H., & Grotzinger, J. P. (2002). Sedimentary controls on the formation and preservation of microbial mats in

siliciclastic deposits: A case study from the upper Neoproterozoic Nama Group, Namibia. *PALAIOS*, *17*, 533–544. https://doi.org/10.1669/0883-1351(2002)017,0533:SCOTFA.2.0.CO;2

Petrovich, R. (2001). Mechanisms of fossilization of the soft-bodied and lightly armored faunas of the Burgess Shale and of some other classical localities. *American Journal of Science*, *301*, 683–726. https://doi.org/10.2475/ajs.301.8.683

Picard, A., Gartman, A., Clarke, D. R., & Giruis, P. R. (2018). Sulfate-reducing bacteria influence the nucleation and growth of mackinawite and greigite. *Geochimica et Cosmochimica Acta*, *220*, 367–384. https://doi.org/10.1016/j.gca.2017.10.006

Pósfai, M., & Dunin-Borkowski, R. E. (2006). Sulfides in biosystems. *Reviews in Mineralogy and Geochemistry*, *61*, 679–714.

Raiswell, R., & Berner, R. A. (1985). Pyrite formation in euxinic and semi-euxinic sediments. *American Journal of Science*, *285*, 710–724. https://doi.org/10.2475/ajs.285.8.710

Raiswell, R., Hardisty, D. S., Lyons, T. W., Canfield, D. E., Owens, J. D., Planavsky, N. J., Poulton, S. W., & Reinhard, C. T. (2018). The iron paleoredox proxies: A guide to the pitfalls, problems and proper practice. *American Journal of Science*, *318*, 491–526.

Raiswell, R., Whaler, K., Dean, S., Coleman, M. L., & Briggs, D. E. G. (1993). A simple three-dimensional model of diffusion-with-precipitation applied to localised pyrite formation in framboids, fossils and detrital iron minerals. *Marine Geology*, *113*, 89–100.

Rickard, D., & Luther, G. W., III. (1997). Kinetics of pyrite formation by the H_2S oxidation of iron II monosulphide in aqueous solutions between 25 and 125°C: The mechanism. *Geochimica et Cosmochimica Acta*, *61*, 135–147.

Schiffbauer, J. D., Selly, T., Jacquet, S. M., Merz, R. A., Nelson, L. L., Strange, M. A., Cai, Y., & Smith, E. F. (2020). Discovery of bilaterian-type through-guts in cloudinomorphs from the terminal Ediacaran Period. *Nature Communications*, *11*, 205. https://doi.org/10.1038/s41467-019-13882-z

Schiffbauer, J. D., Xiao, S., Cai, Y., Wallace, A. F., Hua, H., Hunter, J., Xu, H., Peng, Y., & Kaufman, A. J. (2014). A unifying model for Neoproterozoic-Palaeozoic exceptional fossil preservation through pyritization and carbonaceous compressions. *Nature Communications*, *5*, 5754. https://doi.org/10.1038/ncomms6754

Seilacher, A. (1999). Biomat-related lifestyles in the Precambrian. *PALAIOS*, *14*, 86–93. https://doi.org/10.2307/3515363

Seilacher, A., & Pflüger, F. (1994). From biomats to benthic agriculture: A biohistoric revolution. In W. E. Krumbein & L. J. Stal (Eds.), *Biostabilization of sediments* (pp. 97–105). Bibliotheks und informations system der Carl von Ossietzky Universität Oldenburg.

Shen, Y., Zhang, T., & Hoffman, P. F. (2008). On the coevolution of Ediacaran oceans and animals. *Proceedings of the National Academy of Sciences of the United States of America*, *105*, 7376–7381.

Slagter, S., Hao, W., Planavsky, N. J., Konhauser, K. O., & Tarhan, L. (2022). Biofilms as agents of Ediacaran-style fossilization. *Scientific Reports*, *12*, 1–9. https://doi.org/10.1038/s41598-022-12473-1

Slagter, S., Tarhan, L. G., Hao, W., Planavsky, N. J., & Konhauser, K. O. (2021). Experimental evidence supports early silica cementation of the Ediacara biota. *Geology*, *49*, 51–55. https://doi.org/10.1130/G47919.1

Steiner, M., & Reitner, J. (2001). Evidence of organic microstructures in Ediacara-type fossils and associated microbial mats. *Geology*, *29*, 1119–1122.

Tarhan, L. G., Planavsky, N. J., Wang, X., Bellefroid, E. J., Droser, M. L., & Gehling, J. G. (2018). The late-stage "ferruginization" of the Ediacara Member (Rawnsley Quartzite, South Australia): Insights from uranium isotopes. *Geobiology*, *16*, 35–48. https://doi.org/10.1111/gbi.12262

Tarhan, L. G., Droser, M. L., Gehling, J. G., & Dzaugis, M. P. (2015). Taphonomy and morphology of the Ediacara from genus *Aspidella*. *Precambrian Research*, *257*, 124–136.

Tarhan, L. G., Hood, A. V. S., Droser, M. L., Gehling, J. G., & Briggs, D. E. G. (2016). Exceptional preservation of soft-bodied Ediacara biota promoted by silica-rich oceans. *Geology*, *44*, 951–954. https://doi.org/10.1130/G38542.1

Tarhan, L. G., Hood, A. V. S., Droser, M. L., Gehling, J. G., Briggs, D. E. G., Gaines, R. R., Robbins, L. J., & Planavsky, N. J. (2019). Comment: Petrological evidence supports the death mask model fo rthe preservation of Ediacaran soft-bodied organisms in South Australia. *Geology*, *47*, e473. https://doi.org/10.1130/G46326C.1

Tostevin, R., Wood, R. A., Shields, G. A., Poulton, S. W., Guilbaud, R., Bowyer, F., Penny, A. M., He, T., Curtis, A., Hoffmann, K. H., & Clarkson, M. O. (2016). Low-oxygen waters limited habitable space for early animals. *Nature Communications*, *7*, 12818. https://doi.org/10.1038/ncomms12818

Vasconcelos, C., Warthmann, R., McKenzie, J. A., Visscher, P. T., Bittermann, A. G., & von Lith, Y. (2006). Lithifying microbial mats in Lagoa Vermelha, Brazil: Modern Precambrian relics? *Sedimentary Geology*, *185*, 175–183.

Wade, M. (1968). Preservation of soft-bodied animals in Precambrian sandstones at Ediacara, South Australia. *Lethaia*, *1*, 238–267.

Wallace, A. F., De Yoreo, J. J., & Dove, P. M. (2009). Kinetics of silica nucleation on carboxyl- and amine-terminated surfaces: Insights for biomineralization. *Journal of the American Chemical Society*, *131*, 5244–5250.

Wallace, M. W., Hood, A. V. S., Shuster, A., Greig, A., Planavsky, N. J., & Reed, C. P. (2017). Oxygenation history of the Neoproterozoic to early Phanerozoic and the rise of land plants. *Earth and Planetary Science Letters*, *466*, 12–19. https://doi.org/10.1016/j.epsl.2017.02.046

Wilkins, R. T., & Barnes, H. L. (1996). Pyrite formation by reactions of iron monosulfides with dissolved inorganic and organic sulfur species. *Geochimica et Cosmochimica Acta*, *60*, 4167–4179.

Wille, M., Nägler, T. F., Lehmann, B., Schröder, S., & Kramers, J. D. (2008). Hydrogen sulphide release to surface waters at the Precambrian/Cambrian boundary. *Nature*, *453*, 767–769.

Wollanke, G., & Zimmerle, W. (1990). *Petrographic and geochemical aspects of fossil embedding in exceptionally well preserved fossil deposits* (Vol. *69*, pp. 77–97). Universität Hamburg, Geologisch-Paläontologisches Institut, Mitteilungen.

Wood, R. A., Pouton, S. W., Prave, A. R., Hoffmann, K.-H., Clarkson, M. O., Guilbaud, R., Lyne, J. W., Tostevin, R., Bowyer, F., Penny, A. M., Curtis, A., & Kasemann, S. A. (2015). Dynamic redox conditions control late Ediacaran metazoan ecosystems in the Nama Group, Namibia. *Precambrian Research*, *261*, 252–271. https://doi.org/10.1016/j.precamres.2015.02.004

Xiao, S., & Laflamme, M. (2009). On the eve of animal radiation: Phylogeny, ecology and evolution of the Ediacara biota. *Trends in Ecology & Evolution*, *24*, 31–40. https://doi.org/10.1016/j.tree.2008.07.015

Zhu, M., Gehling, J. G., Xiao, S., Zhao, Y., & Droser, M. L. (2008). Eight-armed Ediacara fossil preserved in contrasting taphonomic windows from China and Australia. *Geology*, *36*, 867–870. https://doi.org/10.1130/G25203A.1

SUPPORTING INFORMATION

Additional supporting information can be found online in the Supporting Information section at the end of this article.

How to cite this article: Gibson, B. M., Schiffbauer, J. D., Wallace, A. F., & Darroch, S. A. F. (2023). The role of iron in the formation of Ediacaran 'death masks'. *Geobiology*, *00*, 1–14. https://doi.org/10.1111/gbi.12551